Materials and Design 193 (2020) 108852

Contents lists available at ScienceDirect

Materials and Design

journal homepage: www.elsevier.com/locate/matdes

# The effect of laser scanning strategies on texture, mechanical properties, and site-specific grain orientation in selective laser melted 316L SS

Jithin James Marattukalam [a,*], Dennis Karlsson [b], Victor Pacheco [b], Přemysl Beran [c,e], Urban Wiklund [d], Ulf Jansson [b], Björgvin Hjörvarsson [a], Martin Sahlberg [b]

[a] Department of Physics, Materials Physics, Uppsala University, Box 530, SE-75121 Uppsala, Sweden
[b] Department of Chemistry- Ångström Laboratory, Uppsala University, Box 523, 75120 Uppsala, Sweden
[c] Department of Neutron Physics, Nuclear Physics Institute, ASCR, CZ -25068 Řež, Czech Republic
[d] Department of Engineering Sciences, Applied Materials Science, Uppsala University, Box 534, 75121 Uppsala, Sweden
[e] European Spallation Source ERIC, Box 176, 22100 Lund, Sweden

## HIGHLIGHTS

- Laser scanning strategies strongly influence the crystallographic texture in as-printed components.
- A ⟨100⟩ single crystalline-like texture is obtained in the direction of laser writing.
- Site-specific texture control is achieved by selectively switching laser scanning strategies.

## GRAPHICAL ABSTRACT

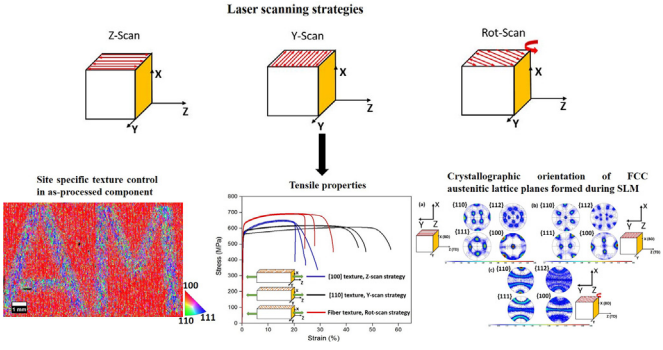


## ARTICLE INFO

*Article history:*
Received 13 December 2019
Received in revised form 1 June 2020
Accepted 2 June 2020
Available online 03 June 2020

*Keywords:*
Selective laser melting
Texture
Austenitic stainless steel
Solidification microstructures

## ABSTRACT

Selective laser melting has been used to demonstrate the striking effect of laser scanning strategies on the crystalline texture in 316L SS. The aligned crystal orientation along the tensile direction (*Z*-axis) could be varied using the scanning strategy. A strong ⟨100⟩ single crystalline-like texture is obtained in the direction of the laser scan and a ⟨110⟩ texture was observed in the build direction when using a bidirectional scan without rotation. Fiber texture was observed along the tensile direction when the bi-directional laser scanning vectors were rotated by 67° (Rot-scan) for each layer. The study highlights a correlation between laser scanning strategies with resulting textures, microstructure, and mechanical properties in as-printed bulk 316L SS. The hardness, Young's modulus, and ultimate tensile strength were significantly influenced by the final microstructure, crystallographic texture, and porosity. Furthermore, the applied laser scanning strategies made it possible to tailor crystallographic textures locally within the component. This was demonstrated by printing characters with a fiber texture, in a matrix with ⟨100⟩ texture parallel to the *Z*-axis.



## 1. Introduction

Additive manufacturing (AM) or 3D printing has become an indispensable tool to fabricate complex geometries, which are often difficult to manufacture by conventional techniques. The process offers cost

* Corresponding author.
*E-mail address:* jithin.marattukalam@physics.uu.se (J.J. Marattukalam).

https://doi.org/10.1016/j.matdes.2020.108852

reduction, product and process redesign, lead time reduction, and flexibility to manufacture parts with desired material properties [1–5]. Additive manufacturing has evolved from a mere prototyping and tooling technique to a direct part manufacturing method over the past few years [6]. A wide variety of materials have been processed through AM, including titanium, stainless steel, aluminum, nickel-based superalloys, etc. [7–10].

Selective laser melting (SLM) is an AM technique where a scanning laser is used to melt along a certain direction in the powder bed. Typically, high cooling rates and high thermal gradients are achieved in the SLM process, which results in a highly anisotropic solidification of the melt pool [11]. The thermal gradient and solidification front velocity can be used to predict the microstructural growth and morphology, while the cooling rate determines the size of the dendrites formed. Process parameters such as laser power, scan speed, hatch spacing, scanning strategies, and even sample orientation in the build plate have been reported to significantly alter the crystallographic texture during the process [12–15]. As crystalline texture is known to affect, e.g., mechanical and corrosion properties of a component, its control can be used to manufacture parts with desired material properties [16]. Several authors have discussed the impact of laser scanning strategy on the obtained texture in Ni-based alloys. For example, unidirectional laser scanning was found to result in a fiber texture, while bidirectional scanning of the laser gave rise to rotated cube-like texture in the printed components [17]. Furthermore, a switching from transverse anisotropic to isotropic and vice-versa has been demonstrated in the SLM of IN738 [18]. Crystallographic texture control in nickel-base superalloy Inconel 718 was demonstrated by varying the energy density input to the powder bed using different electron beam scan strategies to locally change the grain orientation at precise locations in the as-build component [19]. A strong influence of laser scanning strategy on texture has also been observed when processing wide range of other metals and alloys [20–22].

One of the most common alloys is 316L SS, on which influences of scan strategy on texture have been reported by Wei et al. [23]. They showed that orientation of the primary dendrites was at 60° for all deposited layers with unidirectional scanning laser scan, and for bidirectional laser scan, it was found to be 90° in the neighboring layers. Furthermore, in a recent study by Andreau et al. the effect of gas flow and direction of laser scanning on crystallographic texture in 316L SS was discussed [24]. They observed that the crystallographic texture appeared to be dependent on the relative direction of laser scanning and gas flow, which was attributed to an absorbing effect of the metal vapor plume. Scanning in the same direction as the gas flow was found to affect the depth of the melt pool, due to local attenuation of the laser beam's effective energy density transmitted to the powder bed.

The aim of this work is to demonstrate how laser scanning strategy can be used to control texture during SLM, and even obtaining single crystals of 316L SS. The microstructure and crystallographic textures formed during the process are correlated to the mechanical properties. The use of laser scanning strategies to control the final shape of the part and to simultaneously imprint a predesigned spatially resolved crystallographic grain orientation pattern during the SLM process is also demonstrated.

## 2. Materials and methods

316L SS gas atomized powders are produced by EOS, GmBH using industrial-grade feedstock materials. The as-received powder particles were sieved using a 63 μm meshed sieve to remove oversized particles. The sieved powder consists mostly of spherical particles, as shown in Fig. 1. The powder size distribution for 316L SS was determined according to ASTM B822/ISO13320, and the D10, D50 and D90 values are 20 μm, 40 μm, and 60 μm respectively. The chemical composition of the used virgin 316L stainless steel powder is shown in supplementary

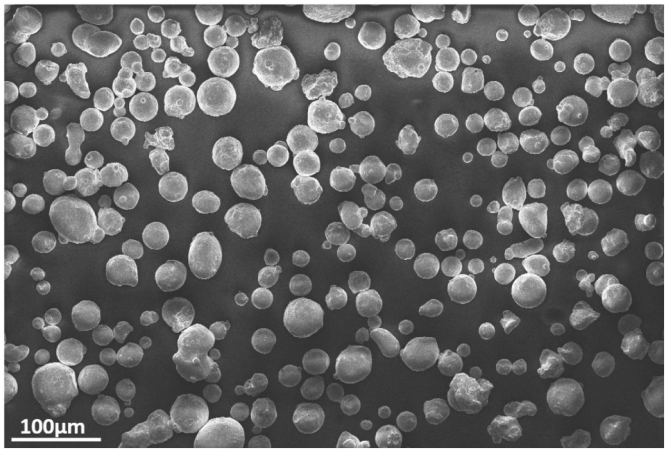


**Fig. 1.** A secondary electron image showing the morphology of gas atomized 316L SS powder.

Table S1. The printing was carried out in an EOS M100 (EOS GmBH, Germany) system equipped with a Yb fiber laser. Different parameters including laser power, scan speed, hatch spacing, and hatch overlap, were varied in order to produce dense and crack free samples. The samples used to study the effect of different scanning strategies were processed using the optimised parameters, with a laser power of 107 W, scan speed of 800 mm/s, and hatch spacing of 70 μm, to obtain the best microstructural features. The thickness was set to 20 μm for each powder layer deposition. The laser spot diameter was 40 μm, and bidirectional laser scanning was used. The process chamber was flushed with argon to minimize the presence of impurities in the material.

Three different scanning strategies were used in the printed parts, as shown in Fig. 2, Z-scan (along the raking direction of the powder bed), Y-scan (perpendicular to the raking direction), and 67° rot-scan with bidirectional laser scanning vectors. The 3D computer-aided design (CAD) models for the tensile samples were generated using Magics software, from Materialise, which is then numerically sliced into a number of layers across the cross-section using EOS RP Tools 1.6 software. These sliced layers are then recreated sequentially on a carbon steel build plate to fabricate the components using an EOS PRINT software.

The samples were cut (XY plane) and the pieces were polished using a series of SiC emery papers, diamond paste, and finally, silicon dioxide to obtain a mirror finish. The samples were etched in diluted aqua regia for the 10 s to reveal the melt pool patterns, which were observed using Olympus AX70 optical microscope. The relative densities of as-printed samples were determined using the Archimedes principle. The weight of the sample ($W_1$) was measured in air at room temperature (RT). The samples were then immersed in water and the weight ($W_2$) was measured at RT. The relative density of the sample was calculated as follows;

$$\text{Relative density}\ (\%) = \left[\frac{(\text{W1 x density of water})}{(\text{W1}-\text{W2})\ \text{x}\ 7.98}\right] \times 100. \quad (1)$$

The density of water at RT was taken to be 0.9978 g/cm$^3$. The theoretical density of 316L SS is taken as 7.98 g/cm$^3$. The weight of the samples was measured using an electronic balance with 0.1 mg accuracy.

Electron backscatter diffraction (EBSD) mapping was carried out using an acceleration voltage of 20 kV and a beam current of 10 nA at 14 mm working distance in a Zeiss Merlin scanning electron microscope (SEM). The samples were mounted at 70° using a pre-tilted sample holder, and the data was recorded in the AZtec HKL software utilizing a Nordlys Max detector. The pole-figures were reconstructed from the EBSD maps using a half-width of 10° to analyze the grain orientation with respect to scan strategies in the printed parts. X-ray diffraction

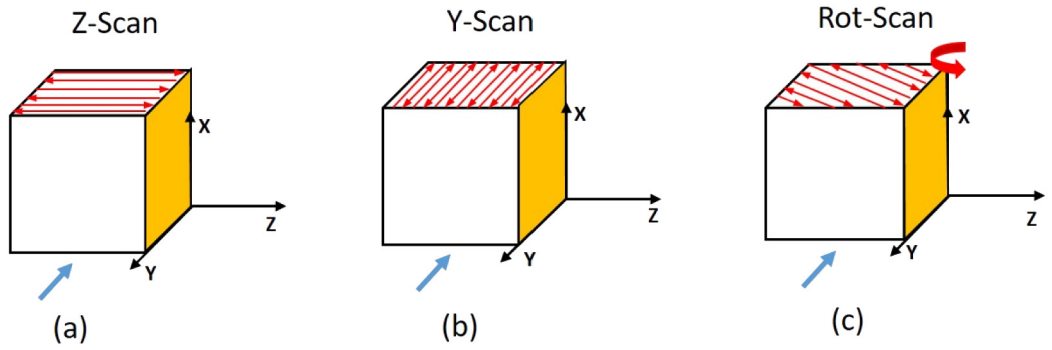


**Fig. 2.** Schematic view of laser scan strategies used for the fabrication of 316L SS samples. (a) laser scan direction along the Z direction, (b) laser scan direction along Y direction, and (c) laser scan rotated by 67° for each layer. Laser scanning strategies are illustrated in the YZ plane. The direction of gas flow is parallel to the Y-axis, indicated by blue arrows. The region marked in yellow illustrates the planes (XY) used for structural investigations.

was performed on the XY planes in the as-processed samples. The measurements were carried out using D8 Bruker Twin-Twin diffractometer, with Cu-Kα radiation operating at 40 kV and 40 mA. 2θ angle was varied from 30° to 100° with a scan rate of one degree per minute.

In order to determine the bulk texture of the as-printed components, neutron diffraction was used, enabling measurements on a large sample volume of $10 \times 10 \times 10$ mm$^3$. This ensures that observations are representative of the whole sample. Samples are fixed on the Euler goniometer and rotated along φ (0–360°) and χ (0–90°) angles with a step of 5°. Variation of neutron diffracted intensities for 4 individual reflections [(111), (200), (220), and (311)] were collected for each orientation on the MEREDIT instrument at the Nuclear Physics Institute, Czech Republic, using a neutron wavelength of 1.46 Å. The data was analyzed using JTEX software [25]. The orientation distribution function (ODF) was calculated for each sample, and pole figures for predefined reflections were calculated for easy comparison of all samples.

Vickers microhardness analysis was conducted on a CM series microhardness indenter using 300 gf (~2.94 N) load and a dwell time of 15 s. The load was chosen to 300 gf to avoid visual perception problems when measuring the length of the indentation tips on the sample, and possibly avoiding potential data scatter [26]. The hardness with standard deviation was determined in all samples. Measurements were performed in the tensile direction (*Z*-axis). Rectangular samples $60 \times 10 \times 10$ mm$^3$ in dimension (see supplementary Fig. S1) were manufactured for the uniaxial tensile test. Each series consisted of 3 samples, which were machined according to ASTM E8M standard dimension with a 20 mm gauge length and 4 mm diameter. The samples were pulled along the tensile direction, as indicated by the *Z*-axis in Fig. 2. The deformation rate was 0.005 mm/s, corresponding to an approximate strain rate of 0.00016/s. To allow estimation of fracture elongation, two lines at 5 mm apart were carefully inscribed on the samples, and the distances were measured before and after the tests (see supplementary Fig. S2).

A possibility of fabricating components with desired geometries and predetermined spatial three-dimensional crystallographic texture by using specific laser scanning strategies was also attempted. To demonstrate site-specific switching of crystallographic textures, a rectangular block with dimensions, $20 \times 10 \times 10$ mm$^3$ was fabricated with the letters AMUU throughout the entire thickness of the block. The *Z*-scan and Rot-scan strategies shown in Fig. 2(a, c) was used to melt the letters and block, respectively.

## 3. Results and discussions

### 3.1. Effect of scan strategies on microstructure and crystallographic texture

X-ray diffraction performed on 316L SS samples with different scan strategies in the XY plane show preferential crystallographic orientations, as seen from Fig. 3. A change in relative intensities was observed for the (200) and (220) peaks when measured in the XY plane (Fig. 3

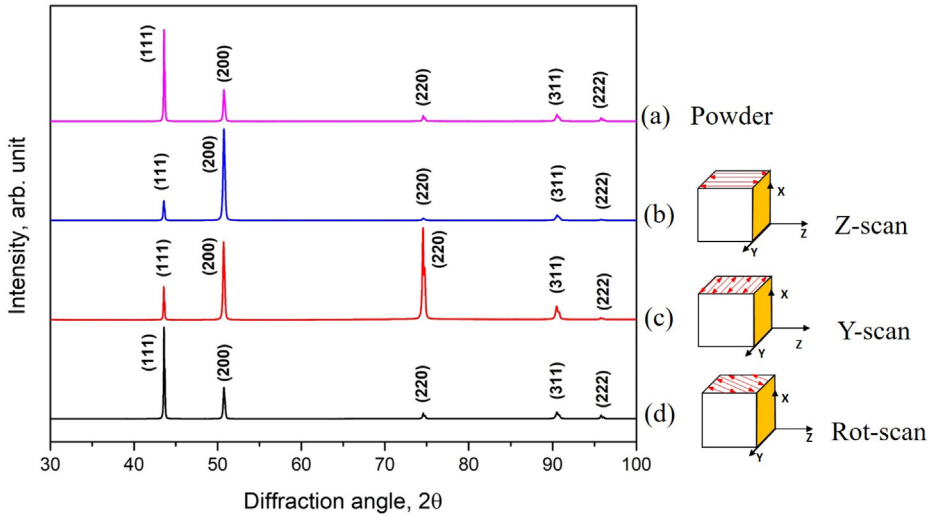


**Fig. 3.** X-ray diffraction patterns of (a) 316L SS powder and in-plane texture measured perpendicular to the XY plane indicated by the yellow area when scanned (b) along the *Z*-axis (c) Y-axis, and (d) 67° rotation.

(b, c)), as compared to the gas atomized powder in Fig. 3(a). This indicated the presence of texture effects in the XY plane when the 'Z' and 'Y' scan strategies were used. However, rotation of scanning vectors by 67° in the sample results in similar intensities as observed in the powder, indicating a random-like distribution of grains in the XY plane (Fig. 3(d)).

The solidification microstructural features obtained during SLM is well studied in literature and is similar to the microstructural aspects observed during the welding process [27]. The microstructural features in the fusion zone are observed to have different morphologies such as planar, cellular, and dendritic structures, and these are governed by temperature gradient, grain growth rate, undercooling, and chemical composition. With increasing constitutional undercooling, the crystallization mode changes from planar to cellular and finally to dendritic solidification mode. A planar growth pattern is observed along line OA and a dendritic growth mode along OB, as illustrated in Fig. 4. The different solidification modes can be attributed to the variation of the temperature distribution across OA and OB within the melt pool. A higher temperature gradient across OA favours planar growth; meanwhile, along OB, the temperature gradient is smaller, which results in the formation of constitutional undercooling zone and induces dendritic growth mode (along OB). Similar observations on grain growth patterns have been previously reported by other researchers on selective laser melting of steels [28–30].

Fig. 5 shows optical images highlighting the melt pool patterns formed during the SLM process. Three types of melt pool patterns are clearly observed with respect to each scan strategy, as shown in Fig. 2. In Fig. 5(a), a nail-head melt pool pattern is observed in the XY plane with respect to a *Z*-scan strategy. This mode of melt pool formation has been reported previously by Fabbro et al. on laser welding, and a similar observation was made by King et al. for powder bed fusion process in 316 L stainless steel [31,32]. A possible reason for the formation of such melt pools is a positive thermocapillary flow (Marangoni effect). This positive convective flow is directed from the center of the melt pool towards the bottom, dissipating most of the heat downwards rather than towards the sides of the melt pool [33]. Columnar grains were found to extend vertically in these melt pool patterns.

Fig. 5(b) shows the melt pool pattern in the XY plane resulting from a Y-scan strategy. Long bands are observed, which are generated due to melt pool flow along the scan. Columnar grains are observed to grow perpendicular to these horizontal band like melt pool traces. This shows that columnar grains mainly grow on a plane perpendicular to the scanning direction, as seen in Fig. 5(b). When the laser scan is rotated by 67° irregular half ellipse melt pool patterns are observed. The grains are also observed to grow and extended beyond the melt pool boundaries along the build direction (X-axis), as shown in Fig. 5(c).

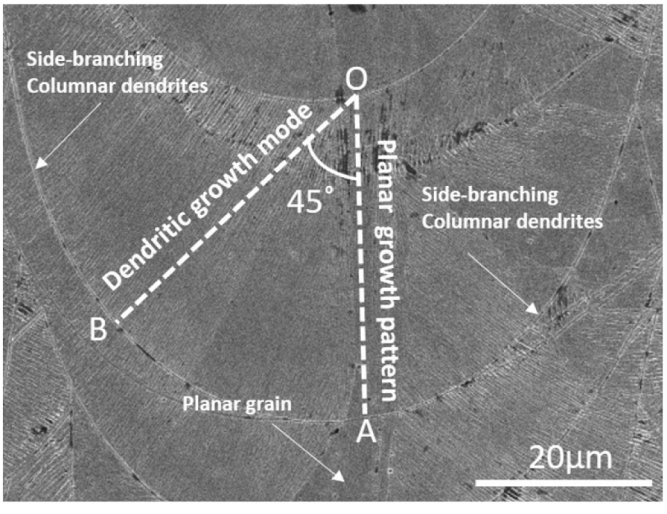


**Fig. 4.** SEM image showing planar and dendritic growth patterns along OA and OB, respectively, which is dependent on the temperature gradient within the melt pool.

The influence of subsequent thermal cycling during multilayer selective laser melting plays a significant role in microstructure formation. An important control parameter that influences the morphology of the solidification microstructure is the ratio between Thermal gradient (TG) and solidification velocity ($V_S$). The effect of this parameter (TG/$V_S$) on multilayer SLM and its role in the formation of a columnar grain structure is elucidated elsewhere [34].

To highlight the observed changes in crystallographic texture and melt pool morphologies with different scanning strategies, detailed microstructural studies were performed using scanning electron microscopy (SEM) and electron backscattered diffraction (EBSD). The melt pool morphologies formed are significantly different with respect to each other and are dependent on the scan strategies used, as illustrated in Fig. 5. When viewed in the XY plane from Fig. 5(a, d), a continuous epitaxial growth of columnar grains is observed along the centerline of the melt pool (indicated by black arrows in Fig. 5(a)). The observed epitaxial growth is a dominant feature in microstructure evolution, and the formation of such feature is attributed to the direction of thermal gradient being vertical along the centreline of the melt pool, as frequently reported in the literature [16,35,36]. However, the growth of these vertical columnar grains is sometimes found to be broken and discontinuous along the melt pool centers. This is possibly due to a dominant lateral migration of the solid-liquid interface, which disrupts their continuous growth [16].The Marangoni flow, which causes the convective heat transfer and fluid flow within the melt pool, could be one of the factors which can influence the heat flux direction due to its heat-mass transfer effect and thereby affect the growth orientation of the dendrites [37,38].

The backward flow of the melt material is the primary heat transfer path, which is also the main direction of solidification. It is observed that a strong ⟨100⟩ crystallographic texture is always obtained along the direction of the laser scan (see Fig. 6(a, d)), in agreement with previous studies [30,37,39]. The 180° degree rotation of the bi-directional laser scan strategy was not found to affect the crystallographic growth of the ⟨100⟩ along the scan direction as multiple rotations of 90° will result in the same crystallographic orientations for cubic symmetries [24]. It is known that in cubic crystal symmetry, ⟨100⟩ has 6 equivalent crystal orientations. If the [001] crystallographic direction is fixed parallel to the scan direction, the other equivalent crystallographic orientations could rotate within the track about a fixed axis when subjected to a radial thermal dissipation [37].

From Fig. 6(d), it is observed that a strong ⟨110⟩ texture is obtained along the build direction and a ⟨100⟩ texture along the scan direction when the scan is bidirectional without rotation. This is an important result obtained from this study, which shows that the growth of the columnar cells preferentially occurred in the ⟨100⟩ crystallographic direction within the plane perpendicular to the scan direction. A recent study by Pham et al. attributed the formation of such a crystallographic texture to the side-branching of columnar dendritic cells in the microstructure [36], as shown in Fig. 4. The underlying mechanism of this phenomenon is due to the misalignment between the existing columnar cells and the thermal gradient, which promotes side-branching due to the perturbations on the existing cells on the sides of the melt pool. The misalignment between the existing thermal gradient and growth direction of columnar cells is a result of a decrease in nucleation energy by conserving crystal orientation between two adjacent melt pools [22]. The side-branching columnar cells grew along a ⟨100⟩ crystallographic direction, inclined about 45° with respect to the build direction, as shown in Fig. 7(a). The orientation relationship of the crystals formed within the melt pool with respect to the scan direction (*Z*-scan) is shown schematically in Fig. 7 for better visualization of single crystalline-like texture formation during SLM.

Fig. 5(b) shows the growth of the columnar grains perpendicular to the elongated band-like melt pool traces when scanned along the Y-axis

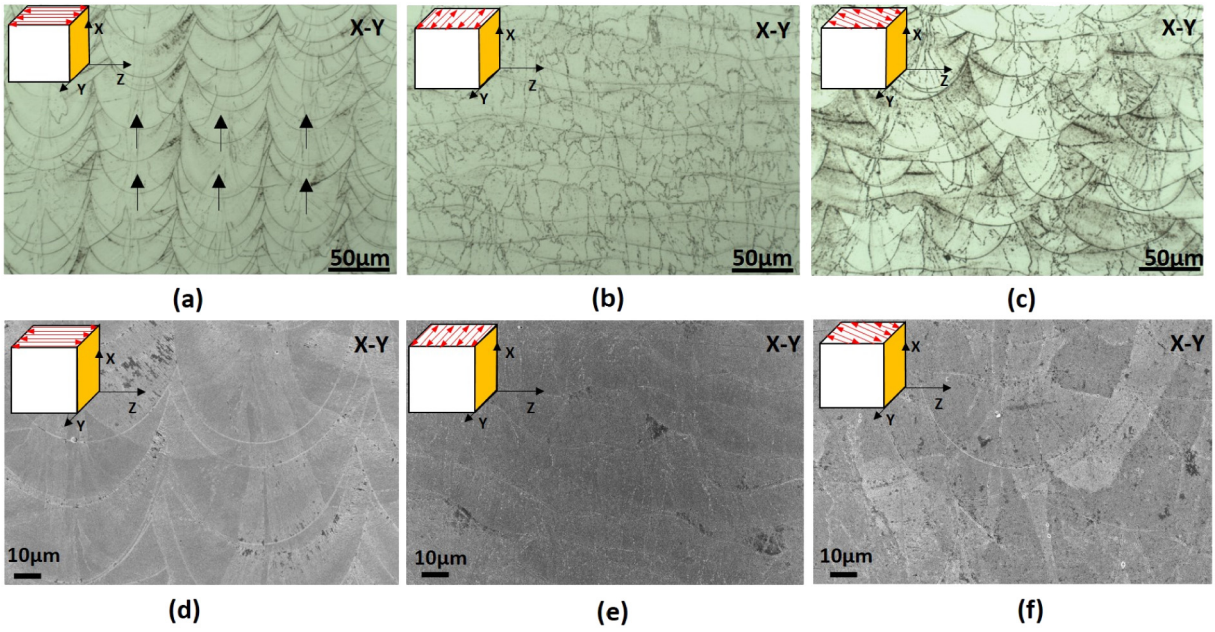


**Fig. 5.** Optical (a–c) and SEM (d–e) images in the XY plane showing morphologies of melt pool patterns and grains formed during selective laser melting of 316L SS austenitic steel with specific scan strategies. (a, d) scan vectors along Z-axis (b, e) scan vectors along Y-axis, and (c, f) scan vectors rotated by 67°. The inset indicates the respective scanning strategies in the YZ plane for each sample. The black arrows in panel (a) indicate the growth direction of columnar lamellar microstructure.

with a bidirectional scan strategy. From Fig. 6 (b, e) it can be observed that the ⟨110⟩ crystallographic direction perpendicular is to the XY plane (along Z-axis, tensile direction). Fig. 5(f) shows the melt pool traces when the scanning vectors are rotated. In the 67° Rot-scan strategy, the melt pool centers of the neighboring layers do not coincide with each other, and the melt pools appear as half ellipses when viewed in the XY plane. They exhibit different morphology in each layer, as observed in Fig. 5(f) and 6(c). The formation of such disoriented melt pool traces in each layer disrupts the development of a single crystalline-like texture with the rotation scan strategy. Pole figures from Fig. 6(f) indicate a strong ⟨110⟩ texture perpendicular to the YZ plane, which is along the direction of the build (X). The diffused rings seen from the {110} pole figure demonstrate a fiber texture along Z (tensile direction), as illustrated in Fig. 6(f).

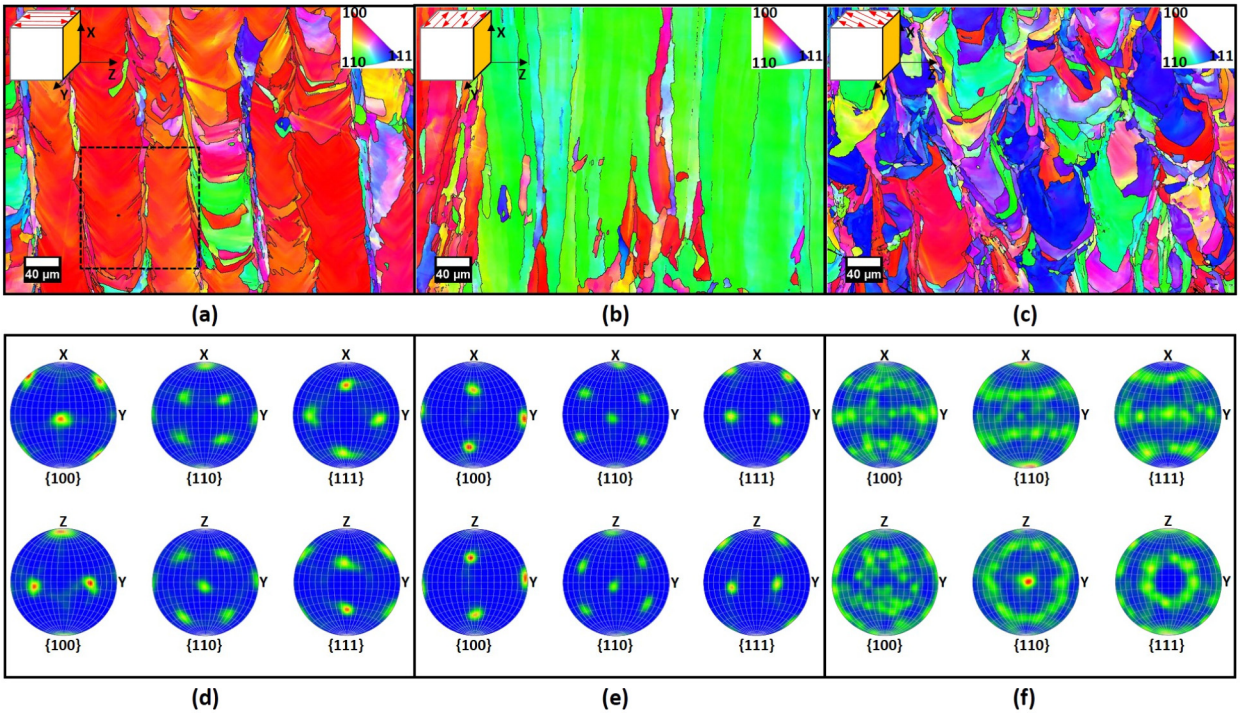


**Fig. 6.** EBSD maps (XY plane) and pole figures in (XY and YZ plane), showing crystallographic grain orientations during selective laser melting of 316L SS austenitic steel when scanned (a, d) along Z-axis, (b, e) Y-axis and (c, f) at 67° rotation. The inset indicates the respective scanning strategies in the YZ plane for each sample.

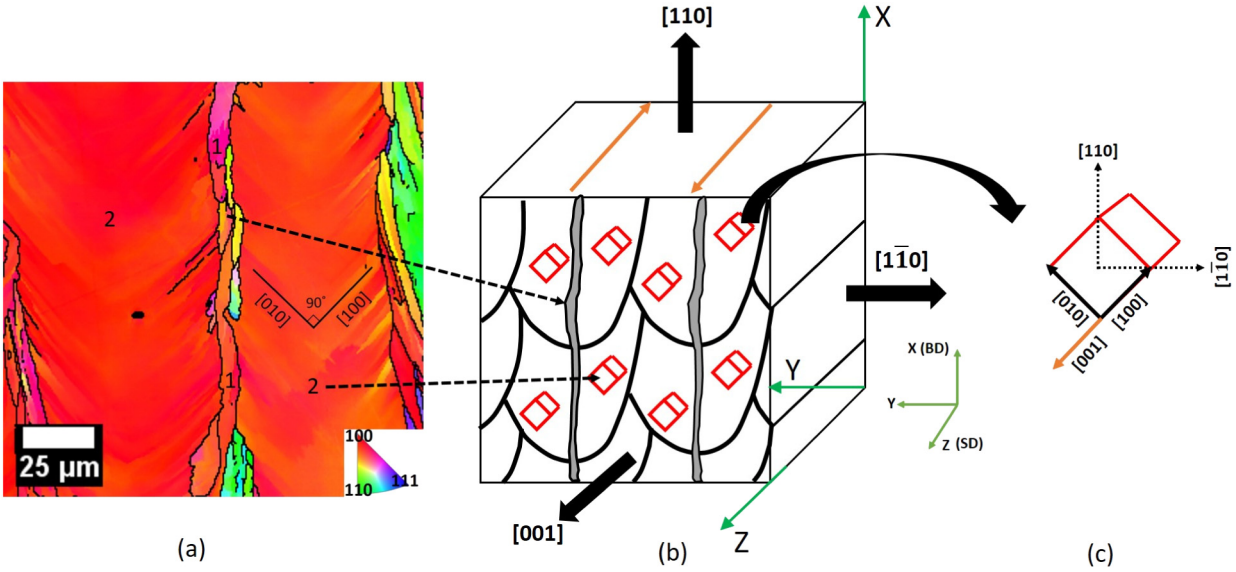


**Fig. 7.** (a) Enlarged view of an EBSD image from the black square in Fig. 6(a) with a chevron-like pattern showing the growth of grains along the ⟨100⟩ crystallographic direction. (b) Schematic illustration showing the melt pool pattern formed during SLM with respect to the bi-directional scanning strategy along the *Z*-axis in the sample. (c) Crystallographic orientations of columnar cells formed within the melt pool during a bidirectional scan without rotation. The build direction (BD) is along the X-axis, and scanning direction (SD) is along the Z-axis, as illustrated above. Region 1 illustrates the continuous epitaxial growth of columnar grains, and region 2 illustrates the side-branching of dendrites growing along ⟨100⟩ crystallographic direction. For further details, please see the text.

Neutron diffraction was used to determine the bulk texture in the samples fabricated using the different scanning strategies. It is observed that the {110} planes are oriented perpendicular to the build direction (X-axis), while the {100} crystallographic planes are perpendicular to the laser scan direction, as shown in Fig. 8 (a, b), which is also in agreement with the EBSD data. Typically, the alignment of the ⟨100⟩ crystallographic direction along the scan direction is explained by the thermal gradient induced during SLM [22,23,40]. The rotation of the scan vectors in every layer by 67° results in a more complex and varied melt pool traces. This scanning strategy results in the fragmentation of the columnar grain structure (see Fig. 6(c)). The specimen built with the rotation scan strategy exhibits a fiber texture with a strong alignment of ⟨110⟩ along the build direction (X-axis) and a random distribution of ⟨100⟩, ⟨110⟩ and ⟨111⟩ crystallographic directions along the tensile direction (*Z*-axis) as illustrated in Fig. 6f and Fig. 8c. The ideal texture components for the as-processed samples are illustrated in supplementary Fig. S3.

The effect of gas flow on microstructure and the crystallographic texture was also investigated in the present study. It was concluded from the neutron diffraction and EBSD studies that a strong ⟨100⟩ single crystalline-like texture always evolves along with the motion of bi-directional laser irrespective of the direction of the scanning (Z scan or Y scan). The melt pool size and shape along the direction of the laser scan was also qualitatively observed to understand the effect of gas flow on as-processed 316L SS, processed with Z and Y scanning strategies (see supplementary Fig. S4). It was concluded from the present study that there was no detectable effect of vapor plume on the crystallographic texture with respect to the direction of the gas flow, in stark contrast to the conclusions made by Andreau et al. [24].

To quantify the size of cellular subgrains, the intragranular cell spacing [41] was evaluated, as illustrated in Fig. 9. The intragranular cell spacing value can be calculated by using the area method by the following equation [29,42]:

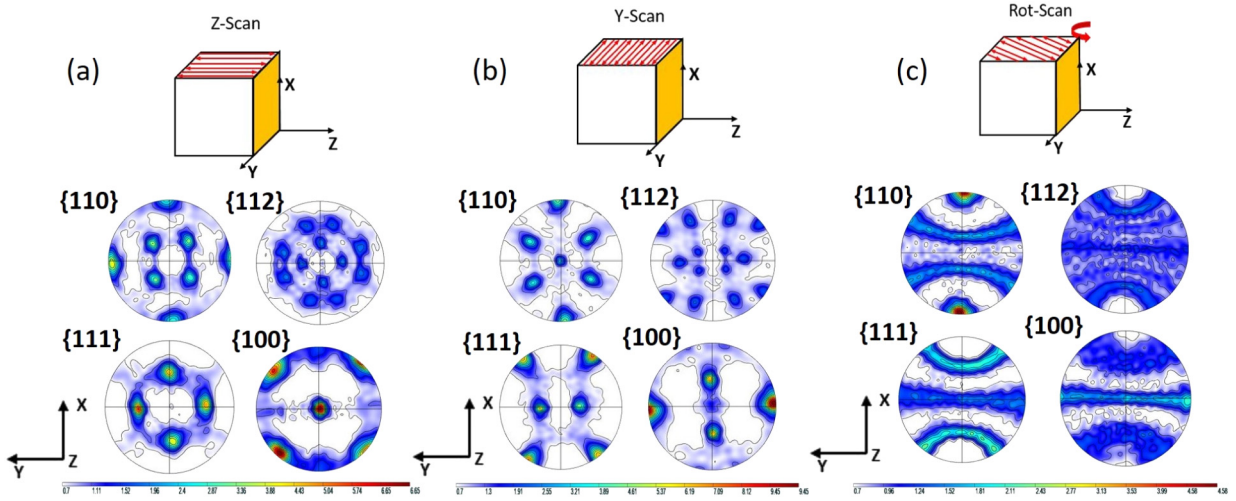


**Fig. 8.** Calculated neutron pole figures showing preferential crystallographic grain orientations, when the scanning vectors are along (a) Z-axis, (b) Y-axis, and (c) rotated by 67° respectively. A strong ⟨100⟩ texture is obtained along the laser scan direction, and ⟨110⟩ texture is observed along the build direction (X-axis).

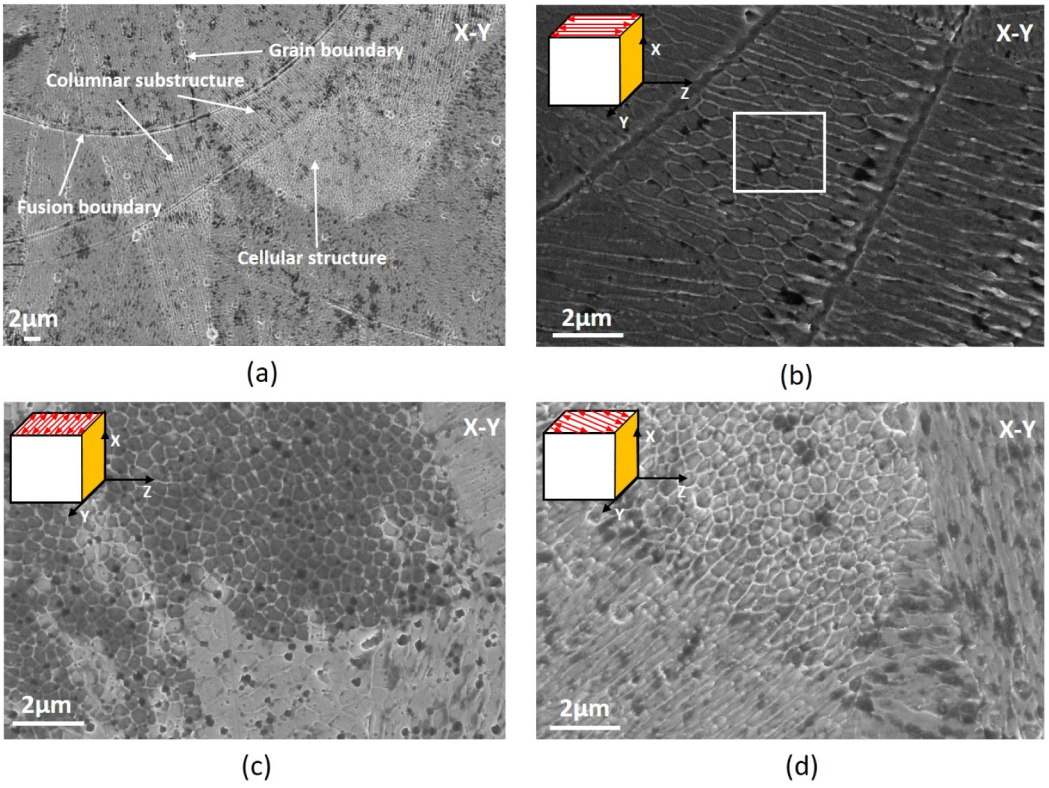


**Fig. 9.** SEM micrographs in the X-Y plane (a) Microstructure at different length scales, which includes melt pool fusion boundaries, grain boundaries, columnar substructure, and cellular structure. High magnification SEM images of the cellular sub-grain structure formed during (b) *Z*-scan (c) Y-scan, and (d) Rot-scan strategies. The inset indicates the respective scanning strategies in the YZ plane for each sample. The white rectangle in Fig. 9(b), indicates the target zone for calculating the intragranular cell spacing.

$$\textit{Intragranular cell spacing} = \frac{1}{M}(A|N)^{1/2} \quad (2)$$

Where 'M,' is the magnification factor of the SEM micrograph, 'N' is the number of cellular subgrains in the target zone, as shown in Fig. 9 (b), indicated by the rectangle and 'A' is the area of the rectangle. The average value of intragranular cell spacing with standard deviation was determined for each scanning strategy by considering different areas in the SEM images with similar magnification having a cellular structure. The intragranular cell spacing showed a decreasing trend when the scanning strategies changed from *Z*-scan (⟨100⟩ single crystalline-like texture) to Y-scan (⟨110⟩ single crystalline-like texture) as shown in Table 1. The change in intragranular cell spacing may be due to a variation of thermal history and degree of undercooling in the melt pool with different scan strategies.

### 3.2. Effect of scan strategies on mechanical properties

Microhardness measurements showed marginal changes in hardness in the tensile direction (*Z*-axis), as shown in Fig. 10. However, no significant differences in hardness were observed between the build and the tensile directions in the as-processed samples despite the difference in microstructure and crystallographic grain orientations. The marginal change in observed hardness could be due to the small variations in intragranular cell spacing, illustrated in Table 1, from 0.40 μm to 0.76 μm. A Hall-Petch type relation can be fitted between hardness and intragranular cell spacing, as illustrated in Fig. 10. Cellular subgrain structures formed during laser powder bed fusion (LPBF) act as barriers for dislocations and induce high densities of entangled dislocations [43–46]. These cellular networks formed in 316L SS during LPBF are found to be stabilized by segregated alloying atoms and minor misorientations developed during rapid solidification of the melt pool [47,48]. The typical size of these cellular structures is <1 μm, with a cell wall thickness of the order of a few hundred nanometres [44]. Owing to their small size, they can provide more barriers for dislocation motion in selectively laser melted austenitic stainless steels than in conventional stainless steels that lack microstructural features at this scale.

Experimentally observed values of Young's modulus in as-processed samples, along with scanning strategies and resulting crystallographic textures, are shown in Table 1. The results show a significant effect of the applied scan strategies on Young's modulus in the samples, measured along the Z-axis. The Young's modulus was observed to change with scanning strategy from 129 ± 3 GPa (Z-scan) to 193 ± 16 GPa (67°Rot-scan), as illustrated in Table 1. Since Young's modulus depends on the strength and density of interatomic forces, its value is sensitive to the atomic arrangement along a specific crystallographic direction [58]. In general, the elastic modulus varies with interatomic distances in a single crystal, and for an FCC system, it is ordered accordingly as $E_{[111]} > E_{[110]} > E_{[100]}$ [59,60]. Since the texture along the tensile direction (*Z*-axis) differs with respect to scanning strategies, the observed variation in Young's modulus is expected, as shown in Table 1.

Fig. 11 shows the combined stress-strain curve for samples printed with different laser scanning strategies. The yield strength was found to increase from 554 ± 5 MPa in samples with [100] texture to 603 ± 2 MPa in samples with fiber texture, as shown in Table 1. The change in tensile yield strength could be due to several factors such as microstructure (intragranular cell spacing), crystallographic texture (Taylor factor), and porosity in as-printed samples. The influence of the above-mentioned factors on the mechanical properties is discussed in the following section.

The mechanical properties of the samples appear to be strongly influenced by the presence of intragranular cellular structures. The observed cellular structures formed, see Fig. 9(b, c, d) result from high cooling rates and non-equilibrium conditions in the SLM process [49]. The morphology of the cellular structure and size of the cells are

**Table 1**
Tensile properties and intergranular cell spacing of AM 316L SS with specific in-plane textures formed with different laser scanning strategies, along the Z-axis.

| Scan strategy | Resulting texture | Young's modulus (GPa) | Yield strength (MPa) | Ultimate tensile strength (MPa) | Elongation at fracture (%) | Intragranular cell spacing (μm) |
|---|---|---|---|---|---|---|
| Z-scan | ⟨100⟩ | 129 ± 3 | 554 ± 5 | 649 ± 3 | 26 ± 1 | 0.76 ± 0.07 |
| Y-scan | ⟨110⟩ | 167 ± 3 | 555 ± 11 | 613 ± 5 | 42 ± 6 | 0.53 ± 0.03 |
| Rot-scan | Fiber | 193 ± 16 | 603 ± 2 | 690 ± 2 | 32 ± 2 | 0.40 ± 0.03 |

influenced by laser scanning strategies, and more specifically, by the resulting temperature gradients during the laser melting process.

The cellular structure exists in the columnar grains and is present as an intragranular feature. Hence, a cellular structure cannot be interpreted as a grain structure because the adjacent cells have similar crystallographic orientation, as previously reported elsewhere [49]. Although cellular structures cannot be considered as grains, they play a significant role in acting as barriers to dislocation motion during deformation. A Hall-Petch type correlation between tensile strength and intragranular cell spacing have been previously reported in [50,51]. Both the yield strength and ultimate tensile strength showed a linear correlation with the reciprocal of the square root of intragranular cellular spacing, indicating the importance of cellular structures in the strengthening of selectively laser melted 316L SS components.

The size of these cellular structures formed during SLM with different scanning strategies is determined using the 'area method' as described above. The mean cellular size is found to vary from 0.76 μm to 0.40 μm, illustrated in Table 1. However, a Hall-Petch type correlation between the yield and ultimate tensile strength with intragranular cell spacing was not observed in the present study. This could be due to the influence of the two other factors (Taylor factor and porosity) as discussed below;

The variation in yield strength can be related to variations in the Taylor factor, 'M' [52], which is related to the flow stress σ by:

$$\sigma = M\alpha bG(\rho)^{1/2} \tag{3}$$

where 'b' is the absolute value of Burgers vector, 'G' is the shear modulus, ρ is the total dislocation density, and α is a constant of the order of 0.2–0.35 [53,54]. Since the Taylor factor is an orientation factor which depends on the texture of the materials and on the crystallographic nature of the assumed slip systems, materials with higher Taylor factors require greater axial stress to be plastically deformed [55]. The Taylor factor distribution for as-processed samples with different scanning strategies along the loading direction (*Z*-axis) is evaluated from EBSD (see supplementary Fig. S5). The Taylor factor distribution is mainly between 2.3 and 2.6 for ⟨100⟩ textured sample (*Z*-scan strategy) along the loading direction (Z-axis). For the fiber textured sample (Rot-scan), the distribution of the Taylor factor became broader and has an average value of 3, along the loading direction (Z-axis). Meanwhile, an increase in the fraction of grains with the Taylor factor over 3.4 is observed for ⟨110⟩ textured sample (Y-scan strategy) along the loading direction (Z-axis). The Taylor factor is minimum for the ⟨100⟩ crystallographic texture in a cubic material (see supplementary Fig. S5(a)), this can partly explain the lower yield strength observed in the as-printed sample with ⟨100⟩ crystallographic texture [56,57]. Meanwhile, a marginal increase in ultimate tensile strength for the sample with ⟨100⟩ texture, when pulled along the Z-axis, could be due to the formation of the columnar lamellar microstructure (CLM) as observed and is indicated by black arrows in Fig. 5(a) and Fig. 7(a). The formation of such microstructural features was found for the first time by Sun et al. during the selective laser melting of austenitic stainless steel [16]. A similar microstructural feature with CLM layers is observed in the sample with the Z-scan strategy, as presented in our study. The CLM layers observed showed a discontinuous and broken pattern along the direction of the build. These microstructural features can act as boundaries between the textured regions and possibly hinder dislocations movements, leading to an increased, ultimate tensile strength.

A third factor influencing the yield and ultimate tensile strength is the difference in porosity [58–60]. The change in porosity and tensile strength for sample made with different scan strategies (top sectional view) during the process are shown in Fig. 12. The relative density and average porosity in as-processed bulk samples determined using the Archimedes principle, as shown in Table S2. A high densification level greater (≥99.5%) was observed in samples. The pores were not evenly distributed throughout the sample and were found to be concentrated more in certain areas as compared to the rest of the sample [61].

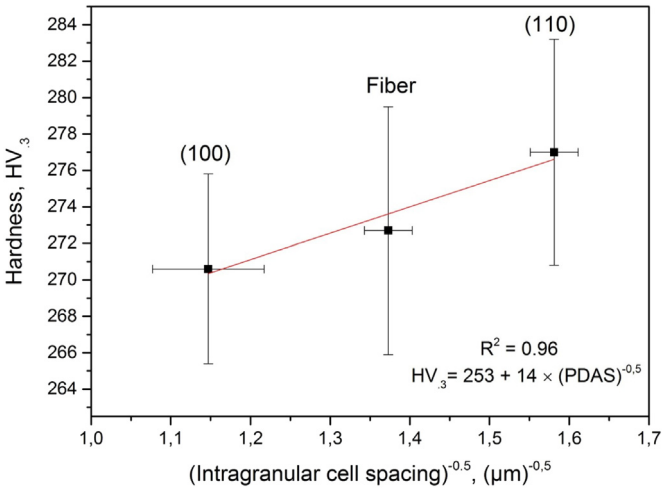


**Fig. 10.** Hardness as a function of the intragranular cell spacing, measured in the tensile direction (*Z*-axis).

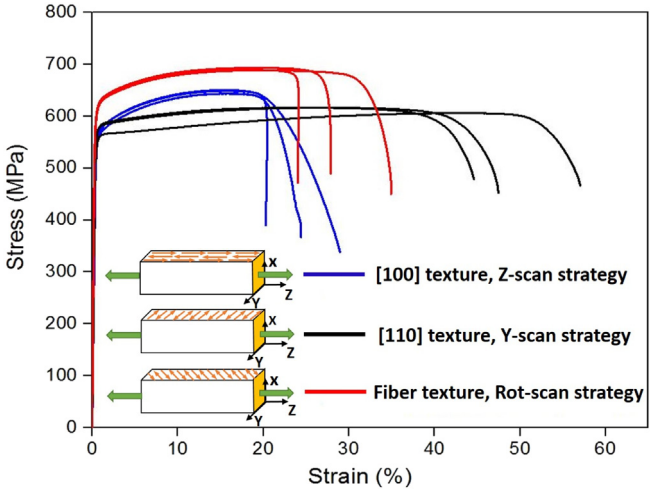


**Fig. 11.** Stress vs. strain in as-printed 316L SS with different scanning strategies. The direction of the applied load is along the Z-axis, which is illustrated by the green arrows in the insets.

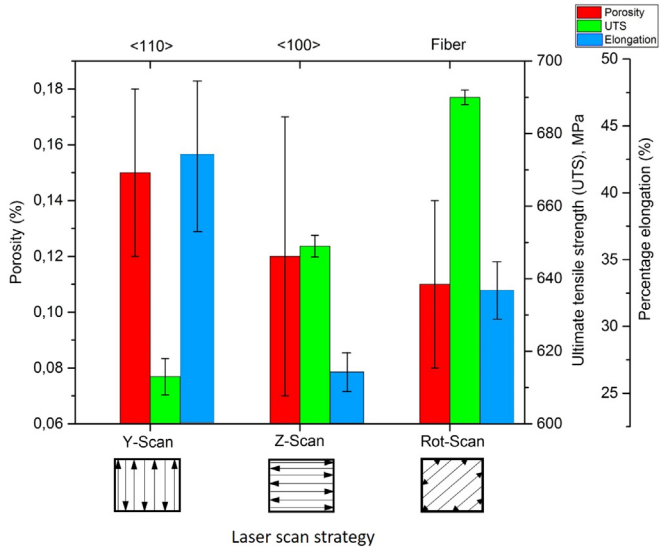


**Fig. 12.** Variation in porosity, ultimate tensile strength, and percentage elongation with different laser scanning strategies during the SLM process, measured along the Z-axis.

From optical microscopy, the highest area fraction of porosity was observed in the Y-scan sample (see supplementary Fig. S6). This increase in the amount of porosity during SLM can be due to the phenomenon of spatter during SLM [62–64]. The amount of spatter generated with respect to laser scanning strategies has been previously reported elsewhere [65–67]. Spatter results in detrimental effects on the components and often results in higher porosity and, consequently, a reduced yield strength. The observed variation in density due to the difference in scanning strategy could partly explain the lower yield and tensile strength in the ⟨110⟩ single crystalline-like textured sample compared to the ⟨100⟩ textured sample as shown in Fig. 12.

The porosity observed in the laser melted samples could also be due to the phenomenon of balling (resulting from the spatter), which was observed at the laser melted surface in the present study. The presence of these micrometer scaled balls on the surface of the laser melted samples can lead to improper powder bed spreading and affect the final part density. The formation of such features could be ascribed to laser-induced melt splashes caused by capillary instability of the melt and is correlated to laser scanning speeds, as previously investigated by Gu et al. [68]. Porosity in the as-processed parts can also arise due to the presence of entrapped gases, resulting from oxide decomposition at high temperatures during the SLM process [69].

An increase in fracture elongation from 26% to 42% was also observed with a change in scanning strategy. A study by Sinha et al. in 316L austenitic stainless steel demonstrated that tensile deformation occurs initially by slip, but at higher strain, deformation occurs by twinning [70]. Grains with ⟨110⟩ and ⟨111⟩ initially oriented along the tensile direction (*Z*-axis) are especially prone to mechanical twinning [71]. This effect will promote strain hardening of the material with the ⟨110⟩ texture and delay the onset of necking, resulting in the excellent elongation during deformation (see supplementary Fig. S7). The mechanical properties with respect to microstructural and texture evolution in deformation twinned austenitic stainless steel has been discussed in detail elsewhere [72,73].

### *3.3. Site-specific crystallographic grain orientation by use of laser scanning strategies*

Finally, as a part of this study, the site-specific crystallographic orientation of grains within a given component was demonstrated by designing a 3D CAD model with box and letters, as shown in Fig. 13(a). From the above discussions, it is observed that strong single crystalline-like and fiber textures could be generated along the tensile direction (Z-axis) by switching the scanning strategies. This knowledge was used to create different textures within the component by assigning a Z-scan and Rot-scan strategy to the box and letters, respectively. The box shows a preferred ⟨100⟩ orientation in the tensile direction, while a fiber texture is observed inside the letters. This is in agreement with the observations shown in Fig. 6(a, c) and further implicates that the texture is changeable within a single component. Additionally, the microstructure and melt pool morphologies formed in the component can be traced back to the initial observations shown in Fig. 5(a, c) and Fig. 6(a, c). Microstructure and texture control in different parts of the component opens up possibilities to achieve tunable properties depending on specific needs for the application [19].

## 4. 5. Conclusions

The present study shows that a suitable combination of laser power, scan speed, and scanning strategy can be used to determine the resulting texture in the SLM processed 316L SS. The growth of columnar grains within the plane perpendicular to the scanning direction was found to be essential for the development of a strong single crystalline-like texture. A strong ⟨100⟩ and ⟨110⟩ single crystalline-like texture was observed in the direction of laser scan and build direction, respectively, in samples printed with a bidirectional scanning strategy without rotation. The rotation of scans by 67° resulted in a mismatch of the positions of melt pool in each layer, which broke the epitaxy of columnar growth and resulted in fiber texture. Furthermore, it was shown that the applied laser scan strategies greatly influenced the mechanical properties. The hardness, Young's modulus, yield strength, and elongation at fracture were influenced by the final microstructure, porosity, and texture formed in these samples. This shows the possibility to

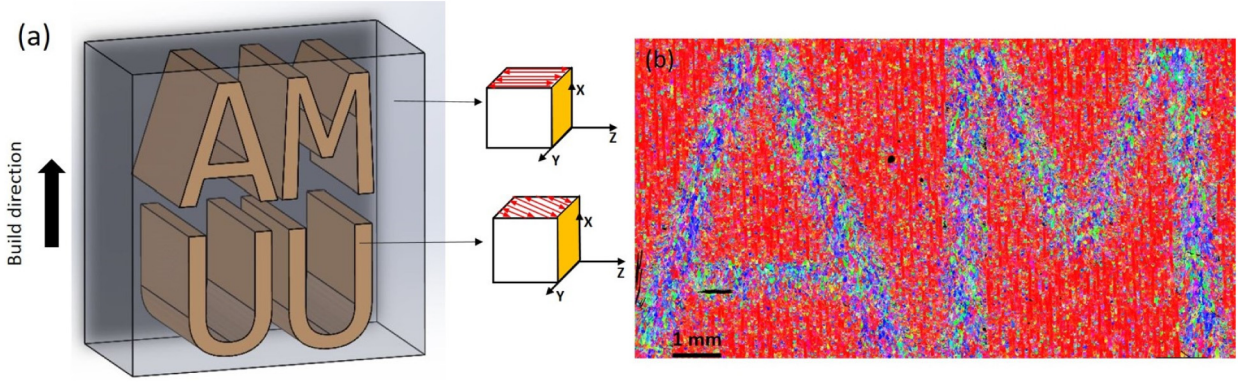


**Fig. 13.** (a) Computer-aided design file with alphabets AMUU and laser scanning strategies Z-scan and 67° Rot-scan used to create site-specific crystallographic grain orientations. (b) EBSD image of SLM component from 13(a) showing a single crystalline-like texture in the rectangular box and fiber texture within the letters AM.

manufacture components with both isotropic and anisotropic properties during a single SLM build. The site-specific control of crystallographic grain orientations within a given metal component was demonstrated by selectively switching laser scanning strategies.

## Data availability

The raw/processed data required to reproduce these findings cannot be shared at this time as the data also forms part of an ongoing study.

## CRediT authorship contribution statement

**Jithin James Marattukalam:** Conceptualization, Investigation, Formal analysis, Writing - original draft, Writing - review & editing. **Dennis Karlsson:** Investigation, Formal analysis, Writing - original draft, Writing - review & editing. **Victor Pacheco:** Investigation, Formal analysis. **Přemysl Beran:** Investigation, Formal analysis. **Urban Wiklund:** Supervision. **Ulf Jansson:** Supervision. **Björgvin Hjörvarsson:** Supervision. **Martin Sahlberg:** Conceptualization, Supervision.

## Declaration of competing interest

The authors declare that they have no known competing financial interests or personal relationships that could have appeared to influence the work reported in this paper.

## Acknowledgments

This research is funded by the Swedish Foundation for Strategic Research (SSF) within the Swedish national graduate school in neutron scattering (SwedNess) and by the Swedish Foundation for Strategic Research (SSF) through the project "Development of Process and Materials in Additive manufacturing", Reference number GMT14-0048. Neutron measurements were performed at the CANAM infrastructure of the NPI CAS Rez and the reactor LVR15 supported through MŠMT project No. LM2015056 and LM2015074. We are also grateful for all the valuable technical support by L. Edlén, N. Johansson, and E. Lindquist.

## Appendix A. Supplementary data

Supplementary data to this article can be found online at https://doi.org/10.1016/j.matdes.2020.108852.

## References

[1] E. Liverani, S. Toschi, L. Ceschini, A. Fortunato, Effect of selective laser melting (SLM) process parameters on microstructure and mechanical properties of 316L austenitic stainless steel, J. Mater. Process. Technol. 249 (2017) 255–263, https://doi.org/10.1016/j.jmatprotec.2017.05.042.
[2] M.M. Kirka, Y. Lee, D.A. Greeley, A. Okello, M.J. Goin, M.T. Pearce, R.R. Dehoff, Strategy for texture management in metals additive manufacturing, JOM 69 (2017) 523–531, https://doi.org/10.1007/s11837-017-2264-3.
[3] M. Rombouts, J.P. Kruth, L. Froyen, P. Mercelis, Fundamentals of selective laser melting of alloyed steel powders, CIRP Ann. 55 (2006) 187–192, https://doi.org/10.1016/S0007-8506(07)60395-3.
[4] M. Badrossamay, T.H.C. Childs, Further studies in selective laser melting of stainless and tool steel powders, Int. J. Mach. Tools Manuf. 47 (2007) 779–784, https://doi.org/10.1016/j.ijmachtools.2006.09.013.
[5] J.P. Kruth, L. Froyen, J. Van Vaerenbergh, P. Mercelis, M. Rombouts, B. Lauwers, Selective laser melting of iron-based powder, J. Mater. Process. Technol. 149 (2004) 616–622, https://doi.org/10.1016/j.jmatprotec.2003.11.051.
[6] W. Gao, Y. Zhang, D. Ramanujan, K. Ramani, Y. Chen, C.B. Williams, C.C.L. Wang, Y.C. Shin, S. Zhang, P.D. Zavattieri, The status, challenges, and future of additive manufacturing in engineering, Comput. Aided Des. (2015)https://doi.org/10.1016/j.cad.2015.04.001.
[7] J.J. Marattukalam, A.K. Singh, S. Datta, M. Das, V.K. Balla, S. Bontha, S.K. Kalpathy, Microstructure and corrosion behavior of laser processed NiTi alloy, Mater. Sci. Eng. C. 57 (2015) 309–313, https://doi.org/10.1016/j.msec.2015.07.067.
[8] E. Louvis, P. Fox, C.J. Sutcliffe, Selective laser melting of aluminium components, J. Mater. Process. Technol. 211 (2011) 275–284, https://doi.org/10.1016/j.jmatprotec.2010.09.019.
[9] F. Abe, K. Osakada, M. Shiomi, K. Uematsu, M. Matsumoto, The manufacturing of hard tools from metallic powders by selective laser melting, J. Mater. Process. Technol. 111 (2001) 210–213, https://doi.org/10.1016/S0924-0136(01)00522-2.
[10] W. Xu, M. Brandt, S. Sun, J. Elambasseril, Q. Liu, K. Latham, K. Xia, M. Qian, Additive manufacturing of strong and ductile Ti–6Al–4V by selective laser melting via in situ martensite decomposition, Acta Mater. 85 (2015) 74–84, https://doi.org/10.1016/j.actamat.2014.11.028.
[11] V. Manvatkar, A. De, T. DebRoy, Heat transfer and material flow during laser assisted multi-layer additive manufacturing, J. Appl. Phys. 116 (2014), 124905. https://doi.org/10.1063/1.4896751.
[12] T. Ishimoto, K. Hagihara, K. Hisamoto, S.-H. Sun, T. Nakano, Crystallographic texture control of beta-type Ti–15Mo–5Zr–3Al alloy by selective laser melting for the development of novel implants with a biocompatible low Young's modulus, Scr. Mater. 132 (2017) 34–38, https://doi.org/10.1016/j.scriptamat.2016.12.038.
[13] K. Kunze, T. Etter, J. Grässlin, V. Shklover, Texture, anisotropy in microstructure and mechanical properties of IN738LC alloy processed by selective laser melting (SLM), Mater. Sci. Eng. A 620 (2015) 213–222, https://doi.org/10.1016/j.msea.2014.10.003.
[14] A.A. Deev, P.A. Kuznetcov, S.N. Petrov, Anisotropy of mechanical properties and its correlation with the structure of the stainless steel 316L produced by the SLM method, Phys. Procedia 83 (2016) 789–796, https://doi.org/10.1016/j.phpro.2016.08.081.
[15] D. Gu, H. Chen, Selective laser melting of high strength and toughness stainless steel parts: the roles of laser hatch style and part placement strategy, Mater. Sci. Eng. A 725 (2018) 419–427, https://doi.org/10.1016/j.msea.2018.04.046.
[16] S.-H. Sun, T. Ishimoto, K. Hagihara, Y. Tsutsumi, T. Hanawa, T. Nakano, Excellent mechanical and corrosion properties of austenitic stainless steel with a unique crystallographic lamellar microstructure via selective laser melting, Scr. Mater. 159 (2019) 89–93, https://doi.org/10.1016/j.scriptamat.2018.09.017.
[17] G.P. Dinda, A.K. Dasgupta, J. Mazumder, Texture control during laser deposition of nickel-based superalloy, Scr. Mater. 67 (2012) 503–506, https://doi.org/10.1016/j.scriptamat.2012.06.014.
[18] F. Geiger, K. Kunze, T. Etter, Tailoring the texture of IN738LC processed by selective laser melting (SLM) by specific scanning strategies, Mater. Sci. Eng. A 661 (2016) 240–246, https://doi.org/10.1016/j.msea.2016.03.036.
[19] R.R. Dehoff, M.M. Kirka, W.J. Sames, H. Bilheux, A.S. Tremsin, L.E. Lowe, S.S. Babu, Site specific control of crystallographic grain orientation through electron beam additive manufacturing, Mater. Sci. Technol. 31 (2014) 931–938, https://doi.org/10.1179/1743284714y.0000000734.
[20] L. Thijs, K. Kempen, J.-P. Kruth, J. Van Humbeeck, Fine-structured aluminium products with controllable texture by selective laser melting of pre-alloyed AlSi10Mg powder, Acta Mater. 61 (2013) 1809–1819, https://doi.org/10.1016/j.actamat.2012.11.052.
[21] L. Thijs, M.L. Montero Sistiaga, R. Wauthle, Q. Xie, J.-P. Kruth, J. Van Humbeeck, Strong morphological and crystallographic texture and resulting yield strength anisotropy in selective laser melted tantalum, Acta Mater. 61 (2013) 4657–4668, https://doi.org/10.1016/j.actamat.2013.04.036.
[22] S.H. Sun, K. Hagihara, T. Nakano, Effect of scanning strategy on texture formation in Ni-25 at.%Mo alloys fabricated by selective laser melting, Mater. Des. 140 (2018) 307–316, https://doi.org/10.1016/j.matdes.2017.11.060.
[23] H.L. Wei, J. Mazumder, T. DebRoy, Evolution of solidification texture during additive manufacturing, Sci. Rep. 5 (2015) 1–7, https://doi.org/10.1038/srep16446.
[24] O. Andreau, I. Koutiri, P. Peyre, J.-D. Penot, N. Saintier, E. Pessard, T. De Terris, C. Dupuy, T. Baudin, Texture control of 316L parts by modulation of the melt pool morphology in selective laser melting, J. Mater. Process. Technol. 264 (2019) 21–31, https://doi.org/10.1016/j.jmatprotec.2018.08.049.
[25] B. Beausir, J.J. Fundenberger, Analysis Tools for Electron and X-ray Diffraction, ATEX-Software, Univ. Lorraine-Metz, 2017.
[26] F. George, V. Voort, R. Fowler, Low-load Vickers microindentation, Adv. Mater. Process. 170 (4) (2012) 28–33.
[27] J.P. Oliveira, T.G. Santos, R.M. Miranda, Revisiting fundamental welding concepts to improve additive manufacturing: from theory to practice, Prog. Mater. Sci. (2019) 100590.
[28] K. Kempen, E. Yasa, L. Thijs, J.-P. Kruth, J. Van Humbeeck, Microstructure and mechanical properties of selective laser melted 18Ni-300 steel, Phys. Procedia 12 (2011) 255–263.
[29] D. Wang, C. Song, Y. Yang, Y. Bai, Investigation of crystal growth mechanism during selective laser melting and mechanical property characterization of 316L stainless steel parts, Mater. Des. 100 (2016) 291–299.
[30] I. Yadroitsev, P. Krakhmalev, I. Yadroitsava, S. Johansson, I. Smurov, Energy input effect on morphology and microstructure of selective laser melting single track from metallic powder, J. Mater. Process. Technol. 213 (2013) 606–613, https://doi.org/10.1016/j.jmatprotec.2012.11.014.
[31] R. Fabbro, Dynamic approach of the keyhole and melt pool behavior for deep penetration Nd-Yag laser welding, AIP Conf. Proc. 1047 (2008) 18–24, https://doi.org/10.1063/1.2999933.
[32] W.E. King, H.D. Barth, V.M. Castillo, G.F. Gallegos, J.W. Gibbs, D.E. Hahn, C. Kamath, A.M. Rubenchik, Observation of keyhole-mode laser melting in laser powder-bed fusion additive manufacturing, J. Mater. Process. Technol. 214 (2014) 2915–2925, https://doi.org/10.1016/j.jmatprotec.2014.06.005.
[33] J. Song, Y. Chew, G. Bi, X. Yao, B. Zhang, J. Bai, S.K. Moon, Numerical and experimental study of laser aided additive manufacturing for melt-pool profile and grain orientation analysis, Mater. Des. 137 (2018) 286–297, https://doi.org/10.1016/j.matdes.2017.10.033.
[34] Y. Liu, Z. Pang, J. Zhang, Comparative study on the influence of subsequent thermal cycling on microstructure and mechanical properties of selective laser melted 316L stainless steel, Appl. Phys. A Mater. Sci. Process. 123 (2017) 688.

[35] A. Basak, S. Das, Epitaxy and microstructure evolution in metal additive manufacturing, Annu. Rev. Mater. Res. 46 (2016) 125–149, https://doi.org/10.1146/annurev-matsci-070115-031728.
[36] M.-S. Pham, B. Dovgyy, P.A. Hooper, C.M. Gourlay, A. Piglione, The role of side-branching in microstructure development in laser powder-bed fusion, Nat. Commun. 11 (2020) 749, https://doi.org/10.1038/s41467-020-14453-3.
[37] X. Zhou, K. Li, D. Zhang, X. Liu, J. Ma, W. Liu, Z. Shen, Textures formed in a CoCrMo alloy by selective laser melting, J. Alloys Compd. 631 (2015) 153–164, https://doi.org/10.1016/j.jallcom.2015.01.096.
[38] D. Dai, D. Gu, Thermal behavior and densification mechanism during selective laser melting of copper matrix composites: simulation and experiments, Mater. Des. 55 (2014) 482–491, https://doi.org/10.1016/j.matdes.2013.10.006.
[39] M. Rappaz, S.A. David, J.M. Vitek, L.A. Boatner, Analysis of solidification microstructures in Fe-Ni-Cr single-crystal welds, Metall. Trans. A. 21 (1990) 1767–1782, https://doi.org/10.1007/BF02672593.
[40] S.-H. Sun, K. Hagihara, T. Nakano, Effect of scanning strategy on texture formation in Ni-25 at.%Mo alloys fabricated by selective laser melting, Mater. Des. 140 (2018) 307–316, https://doi.org/10.1016/J.MATDES.2017.11.060.
[41] Nancy Yang, J. Yee, B. Zheng, K. Gaiser, T. Reynolds, L. Clemon, W.Y. Lu, J.M. Schoenung, E.J. Lavernia, Process-structure-property relationships for 316L stainless steel fabricated by additive manufacturing and its implication for component engineering, J. Therm. Spray Technol. 26 (2016) 610–626, https://doi.org/10.1007/s11666-016-0480-y.
[42] D.G. McCartney, J.D. Hunt, Measurements of cell and primary dendrite arm spacings in directionally solidified aluminium alloys, Acta Metall. 29 (1981) 1851–1863, https://doi.org/10.1016/0001-6160(81)90111-5.
[43] K. Saeidi, X. Gao, Y. Zhong, Z.J. Shen, Hardened austenite steel with columnar subgrain structure formed by laser melting, Mater. Sci. Eng. A 625 (2015) 221–229, https://doi.org/10.1016/j.msea.2014.12.018.
[44] J. Ye, Y.M. Wang, R.T. Ott, Z. Zeng, J.T. McKeown, P.J. Depond, M.K. Santala, T.T. Roehling, T. Zhu, N.P. Calta, M.J. Matthews, Y. Zhang, Z. Li, W. Chen, A.V. Hamza, T. Voisin, Additively manufactured hierarchical stainless steels with high strength and ductility, Nat. Mater. 17 (2017) 63–71, https://doi.org/10.1038/nmat5021.
[45] Y.J. Yin, J.Q. Sun, J. Guo, X.F. Kan, D.C. Yang, Mechanism of high yield strength and yield ratio of 316 L stainless steel by additive manufacturing, Mater. Sci. Eng. A 744 (2019) 773–777, https://doi.org/10.1016/j.msea.2018.12.092.
[46] Z. Sun, X. Tan, S.B. Tor, C.K. Chua, Simultaneously enhanced strength and ductility for 3D-printed stainless steel 316L by selective laser melting, NPG Asia Mater. 10 (2018) 127–136, https://doi.org/10.1038/s41427-018-0018-5.
[47] L. Liu, Q. Ding, Y. Zhong, J. Zou, J. Wu, Y.L. Chiu, J. Li, Z. Zhang, Q. Yu, Z. Shen, Dislocation network in additive manufactured steel breaks strength–ductility trade-off, Mater. Today 21 (2018) 354–361, https://doi.org/10.1016/j.mattod.2017.11.004.
[48] M. Shamsujjoha, S.R. Agnew, J.M. Fitz-Gerald, W.R. Moore, T.A. Newman, High strength and ductility of additively manufactured 316L stainless steel explained, Metall. Mater. Trans. A Phys. Metall. Mater. Sci. 49 (2018) 3011–3027, https://doi.org/10.1007/s11661-018-4607-2.
[49] Y. Zhong, L. Liu, S. Wikman, D. Cui, Z. Shen, Intragranular cellular segregation network structure strengthening 316L stainless steel prepared by selective laser melting, J. Nucl. Mater. 470 (2016) 170–178, https://doi.org/10.1016/j.jnucmat.2015.12.034.
[50] X. Wang, J.A. Muñiz-Lerma, O. Sánchez-Mata, M. Attarian Shandiz, M. Brochu, Microstructure and mechanical properties of stainless steel 316L vertical struts manufactured by laser powder bed fusion process, Mater. Sci. Eng. A 736 (2018) 27–40, https://doi.org/10.1016/j.msea.2018.08.069.
[51] X. Zhang, N. Hansen, Y. Gao, X. Huang, Hall-Petch and dislocation strengthening in graded nanostructured steel, Acta Mater. 60 (2012) 5933–5943, https://doi.org/10.1016/j.actamat.2012.07.037.
[52] N. Hansen, X. Huang, G. Winther, Grain orientation, deformation microstructure and flow stress, Mater. Sci. Eng. A 494 (2008) 61–67, https://doi.org/10.1016/j.msea.2007.10.086.
[53] F.R.N. Nabarro, Z.S. Basinski, D.B. Holt, The plasticity of pure single crystals, Adv. Phys. 13 (1964) 193–323.
[54] R. Neuhaus, C. Schwink, On the flow stress of [100]-and [111]-oriented Cu-Mn single crystals: a transmission electron microscopy study, Philos. Mag. A. 65 (1992) 1463–1484.
[55] H. Mecking, U.F. Kocks, C. Hartig, Taylor factors in materials with many deformation modes, Scr. Mater. 35 (1996) 465–471, https://doi.org/10.1016/1359-6462(96)00137-6.
[56] K. Yvell, Experimental Studies of Deformation Structures in Stainless Steels Using EBSD, KTH Royal Institute of Technology, 2018 63 (2018. doi:urn:nbn:se:kth:diva-227663).
[57] N. Hansen, X. Huang, Microstructure and flow stress of polycrystals and single crystals, Acta Mater. 46 (1998) 1827–1836, https://doi.org/10.1016/S1359-6454(97)00365-0.
[58] G.L. Hao, Q.P. Xu, H. Wang, X.Y. Li, Effect of pore structure on mechanical properties of porous TiAl, Mater. Sci. Technol. (United Kingdom). 32 (2016) 1592–1596, https://doi.org/10.1080/02670836.2015.1132588.
[59] A.E. Wilson-Heid, T.C. Novak, A.M. Beese, Characterization of the effects of internal pores on tensile properties of additively manufactured austenitic stainless steel 316L, Exp. Mech. (2018)https://doi.org/10.1007/s11340-018-00465-0.
[60] B. Gorny, T. Niendorf, J. Lackmann, M. Thoene, T. Troester, H.J. Maier, In situ characterization of the deformation and failure behavior of non-stochastic porous structures processed by selective laser melting, Mater. Sci. Eng. A 528 (2011) 7962–7967, https://doi.org/10.1016/j.msea.2011.07.026.
[61] S.M. Yusuf, Y. Chen, R. Boardman, S. Yang, N. Gao, Investigation on porosity and microhardness of 316L stainless steel fabricated by selective laser melting, Metals (Basel) 7 (2017) 64.
[62] Y. Liu, Y. Yang, S. Mai, D. Wang, C. Song, Investigation into spatter behavior during selective laser melting of AISI 316L stainless steel powder, Mater. Des. 87 (2015) 797–806, https://doi.org/10.1016/j.matdes.2015.08.086.
[63] A.R. Nassar, M.A. Gundermann, E.W. Reutzel, P. Guerrier, M.H. Krane, M.J. Weldon, Formation processes for large ejecta and interactions with melt pool formation in powder bed fusion additive manufacturing, Sci. Rep. 9 (2019) 5038, https://doi.org/10.1038/s41598-019-41415-7.
[64] M. Dal, V. Gunenthiram, R. Fabbro, I. Koutiri, F. Coste, P. Peyre, M. Schneider, Experimental analysis of spatter generation and melt-pool behavior during the powder bed laser beam melting process, J. Mater. Process. Technol. 251 (2017) 376–386, https://doi.org/10.1016/j.jmatprotec.2017.08.012.
[65] A.B. Anwar, Q. Pham, Effect of inert gas flow velocity and unidirectional scanning on the formation and accumulation of spattered powder during selective laser melting, Proc. 2nd Int. Conf. Prog. Addit. Manuf. (pro-AM 2016), 2016.
[66] A. Bin Anwar, I.H. Ibrahim, Q.-C. Pham, Spatter transport by inert gas flow in selective laser melting: a simulation study, Powder Technol. 352 (2019) 103–116, https://doi.org/10.1016/j.powtec.2019.04.044.
[67] T. Heeling, M. Gerstgrasser, K. Wegener, Investigation of Selective Laser Melting Spatter Characteristics for Single-and Multi-Beam Strategies Using High Speed Imaging, in: n.d.
[68] D. Gu, Y. Shen, Balling phenomena in direct laser sintering of stainless steel powder: metallurgical mechanisms and control methods, Mater. Des. 30 (2009) 2903–2910.
[69] X. Gong, T. Anderson, K. Chou, Review on powder-based electron beam additive manufacturing technology, in: ASME/ISCIE 2012 Int. Symp. Flex. Autom., American Society of Mechanical Engineers Digital Collection, n.d.: pp. 507–515.
[70] S. Sinha, J.A. Szpunar, N.A.P. Kiran Kumar, N.P. Gurao, Tensile deformation of 316L austenitic stainless steel using in-situ electron backscatter diffraction and crystal plasticity simulations, Mater. Sci. Eng. A 637 (2015) 48–55, https://doi.org/10.1016/j.msea.2015.04.005.
[71] X. Wang, J.A. Muñiz-Lerma, O. Sanchez-Mata, M. Attarian Shandiz, N. Brodusch, R. Gauvin, M. Brochu, Characterization of single crystalline austenitic stainless steel thin struts processed by laser powder bed fusion, Scr. Mater. 163 (2019) 51–56, https://doi.org/10.1016/j.scriptamat.2018.12.032.
[72] A. Barabi, A. Zarei-Hanzaki, H. Abedi, A. Anoushe, J. Cho, The correlation of macrostructure, microstructure, and texture with room temperature mechanical properties of a twinning-induced plasticity automotive steel after friction stir spot welding/processing, Steel Res. Int. 89 (2018), 1800245. .
[73] A. Barabi, A. Zarei-hanzaki, M. Mosayebi, A. Mohamadizadeh, A.S. Anoushe, Novel analytical approach for evaluating the mechanical properties of friction stir spot joints through constitutive modeling, Eng. Fract. Mech. 216 (2019) 106522, https://doi.org/10.1016/j.engfracmech.2019.106522.